https://doi.org/10.5194/egusphere-2026-4696
Preprint. Discussion started: 18 August 2026

Land-Surface Sensitivity and Climate Variability Shape Global Wet-Dry Regime Transitions

Muhammad Abrar Faiz[1]†, Liangliang Zhang[1]†, Dong Liu[1,2,34*], Qiang Fu[1*], Mo Li[1*], Xiaochen Qi[1], Tianxiao Li[1], Song Cui[1,5],

Affiliations

[1] School of Hydraulic Science & Engineering, Northeast Agricultural University, Harbin, Heilongjiang 150030, China

[2] Joint International Research Laboratory of Habitat Health of Black Soil in Cold Regions, Ministry of Education, Northeast Agricultural University, Harbin, Heilongjiang 150030, China

[3] Key Laboratory of Effective Utilization of Agricultural Water Resources of Ministry of Agriculture and Rural Affairs, Northeast Agricultural University, Harbin, Heilongjiang 150030, China

[4] Heilongjiang Provincial Key Laboratory of Water Resources and Water Conservancy Engineering in Cold Region, Northeast Agricultural University, Harbin, Heilongjiang 150030, China

[5] Research Center for Eco-Environment Protection of Songhua River Basin, Northeast Agricultural University, Harbin, Heilongjiang 150030, China

faiz_ma@neau.edu.cn (†Co-first author)
zhangliangliang@neau.edu.cn (†Co-first author)
liudong@neau.edu.cn (*Co-corresponding author)
fuqiang@neau.edu.cn (*Co-corresponding author)
limo0828@neau.edu.cn
z11745@neau.edu.cn
litianxiao@neau.edu.cn
cuisong-bq@neau.edu.cn

Abstract

Hydroclimatic change is commonly assessed using gradual wetting or drying trends, yet many regions may shift among persistent wet, persistent dry, and transitional wet-dry states. The global geography of these regime transitions and their associations with land-surface conditions and climate variability remain insufficiently quantified. This study aimed to identify global wet-dry regime transitions across historical and future periods and to evaluate how these transitions relate to land-surface characteristics and large-scale climate variability. A stage-focused standardized index was developed to estimate terrestrial water-storage anomalies from monthly water-balance components, including precipitation, evapotranspiration, and runoff. The index was applied to global gridded observations from 1979 to 2023 and to CMIP6 projections. Four hydroclimatic regimes were classified: wet-gets-wetter, dry-gets-drier, wet-gets-dry, and dry-gets-wet. Land-cover diagnostics and large-scale climate indices were used to examine associations among observed transitions, land-surface conditions, and ocean-atmosphere variability. Drying covered 52.9% of the global land area during 1979-2000, with persistent drying as the dominant regime. From 1979-2000 to 2001-2023, persistent drying remained the largest category but declined to 28.7%, followed by wet-gets-dry, wet-gets-wetter, and dry-gets-wet regimes, covering 22.7%, 24.4%, and 24.3% of global land, respectively.

https://doi.org/10.5194/egusphere-2026-4696
Preprint. Discussion started: 18 August 2026

Land-surface diagnostics showed stronger drying in croplands and urban areas, larger dry-to-wet transitions in wetlands, and elevated wet-to-dry transitions in barren regions. Climate diagnostics indicated that internal variability was linked to large-scale ocean-atmosphere patterns, with the strongest association for the Arctic Oscillation and weaker but spatially coherent associations with the Pacific Decadal Oscillation, North Atlantic Oscillation, and Southern Oscillation Index. Under SSP585, the CMIP6 ensemble mean indicated an increase in wet-gets-wetter regimes to 35.2% by 2081-2100 and a reduction in transitional regimes. These findings provide a global diagnostic framework for identifying wet-dry regime transitions and highlight regions where land-surface sensitivity and climate variability may amplify persistent drying, hydroclimatic instability, and risks to future adaptation.

Keywords: Climate; Drought; CMIP6; Sustainability

INTRODUCTION

Droughts are characterized by extended periods of water deficit (*1*) and can severely affect regional economies, ecosystems, and public health (*2–4*). They often arise from global-scale climate variability involving ocean–atmosphere interactions, which drive their development and persistence across seasonal, interannual, and decadal timescales (*5*). Climate change and global warming can exacerbate the risks of droughts and floods (*6*, *7*). The "dry gets drier (DD), wet gets wetter (WW)" paradigm has recently received considerable attention (*8–10*). Studies have been conducted on the concept of the DD–WW paradigm for historical and future periods and have revealed that certain uncertainties persist in characterizing past changes (*7*, *11*), with evidence supporting the DD–WW paradigm derived from oceanic data rather than land observations (*5*, *12*). For example, Greve et al. (2014) analyzed hydrological datasets and reported that only 10.8% of the global land area exhibited a distinct DD–WW pattern (*10*). Feng and Zhang (2015) reported that only 15.12% of cases followed the DD–WW paradigm, based on soil moisture (SM) data (*13*). These studies highlight the complexity of land-use changes indicated by the DD–WW paradigm. Thus, additional analysis is required to better understand the DD–WW paradigm for effective water resource management strategies.

The selection and diversity of methodologies are key challenges that can lead to variability and uncertainty in analyses (*10*, *13–15*). The present study employs a storage-residual signal derived from the monthly water budget, which utilizes precipitation, actual evapotranspiration (AET), and runoff. Furthermore, it integrates the storage-centric standardized index (SPEI-SR) to assess dryness and wetness, as well as their transitions. This approach investigates the storage residual driver and its potential regime shifts, thus providing a novel perspective on the coupling between climatic and hydrological processes over land.

Unlike previous studies on the DD–WW paradigm, our analysis incorporated outputs from Coupled Model Intercomparison Project Phase 6 (CMIP6) models across different shared socioeconomic pathways (SSPs), which rely primarily on historical observations. Using SPEI-SR calculations, our methodology enabled us to quantify trends in dryness and wetness under the DD–WW paradigm. Using this approach, the outputs represented current and future transitions under different climate scenarios, thereby comprehensively evaluating the suitability of the paradigm. We classified land areas into four hydroclimatic transition states: persistent wetting, persistent drying, wet-to-dry reversal, and dry-to-wet recovery. Our goals are to: i) quantify the global and regional extent of these states; ii) determine whether transition behaviors vary across different land cover and land use types; and iii) explore how transition variability relates to large-scale ocean–atmosphere modes. By connecting these transition diagnostics to land-surface and climate-system contexts, we established a framework for understanding where and

https://doi.org/10.5194/egusphere-2026-4696
Preprint. Discussion started: 18 August 2026

why drought-related hydroclimatic changes are intensifying, reversing, or recovering worldwide.

MATERIALS AND METHODS

Hydroclimatic datasets

Historical reanalysis data (ERA5) and future climate model outputs were used to study the DD–WW paradigm. We used the CMIP6 models under seven SSPs: 245 and 585 from 2023 to 2099 (Table S1). The models were interpolated to a resolution of 0.25° to match the historical datasets. In addition, we utilized the TerraClimate global monthly dataset for climate and water-balance data, obtained from the University of Idaho Climatology Lab via https://www.climatologylab.org/terraclimate.html, to derive the aridity index-based DD–WW paradigm. This dataset offers continuous fields on a ~1/24° (~4 km) grid from 1979 to the current year, and is detailed in (*16*). It includes variables such as precipitation (P), reference potential evapotranspiration (PET) calculated using the Food and Agricultural Organization of the United Nations (FAO-56) Penman–Monteith method, AET, runoff (Q) derived within TerraClimate's monthly water-balance framework, and SM. Furthermore, to capture land surface feedback and understand water balance dynamics, precipitation and evaporation anomalies were analyzed along with SM and runoff data. We also evaluated land-surface effects on hydroclimatic transition states using annual Moderate Resolution Imaging Spectroradiometer (MODIS) land-cover data from 2001 to 2023, assigning each grid cell to its dominant land-cover class across the analysis period. These land-cover classes were grouped into broad categories, such as forest, shrub/grass/savanna, wetland, cropland, urban, and barren land, for comparison with the mapped transition states. Irrigation intensity was assessed using data from the FAO Global Map of Irrigation Areas. Gridded areas equipped for irrigation were used to classify irrigation levels and to derive cropland-specific gradients. To study large-scale climatic influences, we incorporated monthly and seasonal climate indices representing key ocean–atmosphere variability modes, including the Pacific Decadal Oscillation (PDO), Arctic Oscillation (AO), Northern Oscillation Index (NOI), and gridded Southern Oscillation Index (SOI). PDO was analyzed as a monthly time series, AO as a monthly atmospheric index, NOI as a seasonal index, and SOI as a gridded anomaly field. These datasets helped us link interannual variations in the proportions of the WW, DD, WD, and DW states to broad-scale atmospheric and oceanic variability.

Storage-centric standardized index

We diagnosed drought (DD–WW paradigm) using a storage-residual signal derived from the monthly water budget: precipitation minus AET minus runoff (Equation 1). In physical terms, this metric reflects the amount of water added to or depleted from terrestrial storage, primarily through SM and seasonal snow. We then created a multi-month signal by summing this residual over fixed periods (such as 3 and 12 months) and converted it into a standardized index called SPEI-SR. Standardization was based on each grid cell's long-term baseline (1979–2023), which enabled comparisons across space and time. Negative values indicated storage deficits or drought, whereas positive values indicated storage gains or increased wetness. Considering AET as an indicator of plant water stress under atmospheric demand and moisture limitation, and removing runoff, filters out quick-flow losses and focuses the analysis on root-zone storage relevant to vegetation and low flows. The resulting storage-residual tendency is:

$$R_t = P_t - \mathrm{AET}_t - Q_t \quad (1)$$

https://doi.org/10.5194/egusphere-2026-4696
Preprint. Discussion started: 18 August 2026

We standardized the accumulated R_t k-month sums using a Gaussian approximation, which is reasonable for aggregated hydroclimatic anomalies and helps avoid parametric misspecification, as alternative month-by-month parametric fits (e.g., log-logistic) produce similar z-scores for 3–12-month windows.

(i) *k-month accumulation*

$$S_t^{(k)} = \sum_{i=0}^{k-1} R_{t-i} \tag{2}$$

(ii) *Standardization*

$$\text{SPEI-SR}_t^{(k)} = \Phi^{-1}\left(F_m\left(S_t^{(k)}\right)\right), \quad m = \text{month}(t) \tag{3}$$

where F_m is the baseline CDF for the calendar month m, and Φ^{-1} is the standard normal quantile.

The canonical standardized precipitation evapotranspiration index (SPEI) employs P−PET with a monthly probability model, often a log-logistic distribution, mapped onto a standard normal distribution. However, the choice and formulation of PET can introduce uncertainty and artifacts related to warming into drought assessments, particularly in arid and energy-limited environments. Using AET avoids reliance on PET methods and directly indicates actual evaporative losses under moisture limitations. This approach aligns with existing AET-based drought indicators, such as the Evaporative Stress Index (*17*), and with storage-based drought assessments that utilize the Gravity Recovery and Climate Experiment terrestrial water storage deficits (*18*), both of which emphasize hydrological impacts over potential demand. Our method applies SPEI-like standardization to a residual storage driver, supplements meteorological indices, and provides a more relevant perspective for ecohydrology.

Aridity indices

The United Nations Environment Programme (UNEP) aridity index uses annual sums, defined as $AI_y = \frac{\sum_{t\in y} P_t}{\sum_{t\in y} PET_t}$. Here, P and PET are the monthly precipitation and potential evapotranspiration, averaged across years of $\overline{AI}$ and used to classify land surfaces in to the following categories: Hyper-arid ($\overline{AI} < 0.03$), Arid ($0.03 \le \overline{AI} < 0.2$), Semi-arid ($0.2 \le \overline{AI} < 0.5$), Dry sub-humid ($0.5 \le \overline{AI} < 0.65$), and Humid ($\overline{AI} \ge 0.65$). Regions with $\overline{AI} < 0.65$ are referred to as "drylands." To attribute changes in runoff and SM, the predictand $Y_t \in \{Q'_t, SM'_t\}$ was regressed on contemporaneous and antecedent driver anomalies up to a lag of $L = 6$ months:

$$Y_t = \alpha + \beta_0^{(E)}\, PET'_t + \beta_0^{(P)}\, P'_t + \sum_{\ell=1}^{L}\left(\beta_\ell^{(E)}\, PET'_{t-\ell} + \beta_\ell^{(P)}\, P'_{t-\ell}\right) + \varepsilon_t \tag{4}$$

We then decomposed the fitted signal into a direct component $D_t = \beta_0^{(E)}\, PET'_t + \beta_0^{(P)}\, P'_t$ and a memory (lagged) component $L_t = \sum_{\ell=1}^{L}\left(\beta_\ell^{(E)}\, PET'_{t-\ell} + \beta_\ell^{(P)}\, P'_{t-\ell}\right)$, with pathway trends $\hat{\beta}_{\text{dir}} = \text{slope}(D_t)$, $\hat{\beta}_{\text{lag}} = \text{slope}(L_t)$, and $\hat{\beta}_{\text{tot}} = \hat{\beta}_{\text{dir}} + \hat{\beta}_{\text{lag}}$. Memory timescales are the lags that maximize the Pearson correlation between Y_t and the driver anomalies: $\tau_P = \text{argmax}_{\ell\in\{1,\ldots,L\}}\text{corr}(Y_t, P'_{t-\ell})$ and $\tau_{PET} = \text{argmax}_\ell\text{corr}(Y_t, PET'_{t-\ell})$, with corresponding maxima c_P and c_{PET}. Hydroclimatic transition classes were determined based on the signs of water-state trend changes in grid cells during the baseline and recent periods. Grid cells exhibiting negative trends in both periods were labeled dry–dry (DD), whereas those with positive trends in both periods were labeled wet–wet (WW). Grid cells transitioning from negative to positive

https://doi.org/10.5194/egusphere-2026-4696
Preprint. Discussion started: 18 August 2026

trends were designated as dry–wet (DW), and those shifting from positive to negative trends were labeled wet–dry (WD). The aridity index was independently used to categorize these transition classes across dryland and humid hydroclimatic regimes.

Hydroclimatic transitions under the DD–WW paradigm

We divided the analysis results into 1979–2000 and 2001–2023 datasets. We then grouped regions according to their SPEI-SR trends. Four categories were defined: (1) wet gets wet (WW), (2) dry gets dry (DD), (3) wet gets dry (WD), and (4) dry gets wet (DW). Categories 3 and 4 are transitional categories. Regions with no valid data were excluded from the classification. This methodology produced a detailed spatial representation of hydroclimatic shifts under the DD–WW paradigm. We applied a spatial mask using a shapefile of global boundaries to restrict the analysis to valid land areas. Visualizations of the final classifications were created using a custom color map to emphasize the development of significant and nonsignificant trends. The land area percentages for each category were also calculated. Significant trends prevailed in humid and arid regions, whereas transitional trends were observed in semiarid zones. This enabled a robust examination of changes in hydrological regimes by integrating SPEI-SR trends across both periods to account for temporal variability and the impact of climate change. Historical data spanning 1979–2023 were used as the reference period. Future simulations under the SSPs were divided into two periods, 2041–2060 and 2081–2099, to compute the DD–WW paradigm results and their transitions according to the reference period.

Results

Historical hydroclimatic regime frequencies and DD–WW paradigms

State-space clustering of monthly precipitation, PET, and SM revealed a distinct reorganization of hydroclimatic state residences during the historical period (Fig. S1). Globally, the dry state expands and intensifies along the subtropical belts (typically by +10–30 percentage points [pp]), while wet-state persistence decreases on tropical margins (−10–20 pp); transition months increase across mid–high latitudes. Regionally, the Amazon core remains wet; however, its southern and eastern edges shift from approximately 70–90% wet months to 50–70%, with transitions up by 10–20 pp, and dry pockets reaching 20–40%. In the Sahara–Sahel, the core desert remains approximately 80–100% dry, whereas the Sahelian fringe intensifies from 40–60% to 60–80% dry (+20 pp). The Arctic becomes even more variable, with the transition rising from 60–80% to 80–95%. Western North America shows a strong aridification trend, with dry months increasing from 50–70% to 60–85% (+10–20 pp). Southern Europe shifts from 50–70% to 70–90% dry (+15–25 pp). Across South Asia, wet persistence weakens along the Indo-Gangetic plains (60–80% to 40–60%), while dry periods grow (10–30% to 20–40%), and the transition increases by approximately 10–20 pp. In Australia, the northern and eastern subtropics shift from 60–80% to 70–90% dryness frequency. These patterns are reflected in key land-use areas: the Brazilian agricultural belt experiences a reduction in wet residence frequency (from 60–80% to 40–60%), with dry conditions reaching approximately 20–40%; Southeast Asian agricultural and deforested zones contract from 70–90% to 50–70% wet; urban areas across India record a combined transition and dry increase to approximately 50–70% (+10–20 pp); China's urban regions are dominated by approximately 60–80% transitional conditions, with modest dry gains concentrated in the North China Plain; and Central Africa's deforestation margin sees wet conditions decline from 70–90% to 50–70%, accompanied by a transition of 10–20 pp. These percentage changes indicate hydroclimatic intensification consistent with the dry-gets-drier and wet-gets-wetter

https://doi.org/10.5194/egusphere-2026-4696
Preprint. Discussion started: 18 August 2026

paradigm: increased dry-season persistence driven by strengthening subsidence and atmospheric demand, and a corresponding loss of wet-season persistence as rising PET offsets precipitation gains. Because these metrics measure residence time in wet, dry, and transition states rather than averages alone, they highlight hotspots of regime persistence and volatility that are directly relevant to drought risk, irrigation water needs, runoff reliability, and urban water management security.

The SPEI-SR trends revealed wet (53.1%) and dry (46.9%) areas from 1979 to 2000, whereas the WW–DD transitions indicated transitions from wet to dry (WD) and dry to wet (DW) from 2001 to 2023 (Fig. 1a, b). Persistent drying (DD) became the dominant transition state, covering 30.7% of the global land surface (Fig. 1b). Persistent wetting (WW) accounted for 23.3%, whereas the wet-to-dry (WD) and dry-to-wet (DW) transitions accounted for 23.7% and 22.3%, respectively. These results indicate that recent hydroclimatic changes were characterized not only by persistent drying, but also by substantial reversals between wet and dry phases, underscoring the heterogeneous nature of global hydroclimatic transitions.

Global DD–WW patterns and response times in runoff and SM

Fig. 2(a) shows the UNEP aridity classes, which align with the typical geography of global drylands. There are hyper-arid and arid belts across the Sahara, Arabia, and Central Asia, as well as in interior Australia. Semi-arid and dry sub-humid areas are found along the edges of monsoon zones. Humid conditions are common in parts of South America and Africa, maritime Southeast Asia, and at high northern latitudes. Combining the baseline regime with the sign of the change yields a four-class taxonomy Fig. 2(b). The DD class dominates large parts of the subtropical belts and continental interiors, particularly in the UNEP drylands of H2 and H7 and the interior of H4. The WD class emerges along humid margins and monsoon transition zones, such as the Mediterranean fringe in H5 and parts of South and East Asia near L2 and L4, indicating dynamical drying in previously wet areas. The WW class was most common at high northern latitudes (H3) and within certain monsoon cores. In contrast, the DW class emerged locally in high-latitude transition zones and in select monsoonal domains, where increased moisture supply offsets PET growth. Furthermore, the total modeled trends in Q in Fig. 2(c) show widespread drying across arid belts, especially in H2, H7, and the interior of H4, with some wetting at high latitudes (H3) and in parts of the humid tropics, where precipitation increases exceed PET growth. The total SM trends in Fig. 2(d) closely mirror Q but exhibit a smoother spatial structure and more extensive negative areas within drylands and along monsoon margins, reflecting the integrative nature of SM and vegetation–soil interactions. For example, in H1 (Amazon) and L2 (SE Asia agricultural/deforested regions), mixed Q tendencies coexisted with strong memory signatures, as deep soils and vegetation recycled and stored moisture; localized SM declines in L2 were compatible with deforestation-driven changes in evaporative demand and rooting depth. H2 (Sahara–Sahel) shows coherent negative Q and SM tendencies at the semi-arid to dry sub-humid fringe, aligning with its DD classification, while allowing for local DW pockets driven by circulation variability. H3 (Arctic) presents positive Q tendencies consistent with increasing precipitation, snow-to-rain shifts, and longer liquid seasons, whereas SM patterns reflect the interplay of thaw, drainage, and vegetation changes. H4 (western North America) features widespread runoff and SM drying across the interior drylands, with patchy wetting in the orographic belts. H5 (southern Europe) exhibits a coherent WD signature, consistent with poleward-shifted storm tracks and warmer summers. H6 (South Asia) exhibits mosaics of DW and WD across monsoon transition zones, with signs depending on onset/retreat dynamics and remote SST forcing. H7 (Australia) shows strong contrasts between the arid interior

https://doi.org/10.5194/egusphere-2026-4696
Preprint. Discussion started: 18 August 2026

(drying) and eastern maritime belts (patchy wetting), echoing the known multi-decadal variability.

The response time quantifies the propagation behavior captured by the regressions. τ for Q, relative to P in Fig. 2(e) is generally short (≈1–2 months) across most regions, especially within arid belts (H2 and H7) where runoff adjusts rapidly to precipitation events. τ for Q relative to PET' in Fig. 2(f) is longer (≈3–6 months) and spatially structured, indicating that evaporative demand influences Q primarily via storage-mediated pathways (soil, groundwater, and snow). In humid and cold regions (H1, H3; mountainous parts of H4/H5), τ_PET_Q lengthens as water resides in slow stores before contributing to flow. For SM, τ to P in Fig. 2(g) is short to moderate (≈1–3 months), shortest in arid zones, and lengthens under cool climates or in deeper soils. τ to PET in Fig. 2(h) is the longest of the four (≈4–6 months) over humid and high-latitude regions and in L2–L4, reflecting cumulative drawdown by sustained evaporative anomalies. These timescales are consistent with independent estimates of soil-moisture memory (~1–>6 months) and its projection to streamflow, providing external validity for the attribution. Taken together, the results indicate that direct climate forcing explains most month-to-month Q variability globally, while memory (lagged) contributions and longer τ become prominent in regions where soils, aquifers, and seasonal snow integrate anomalies. The same structure holds for SM, with a stronger imprint of memory in humid and high-latitude climates. This pattern of change aligns with thermodynamic and dynamical expectations. A warming atmosphere increases moisture-holding capacity and PET, thereby amplifying existing dry–wet contrasts (“thermodynamic contrast”). In addition to this primary trend, circulation changes (storm-track shifts, monsoon onset and withdrawal), cryospheric storage–release processes, and land–atmosphere interactions generate regional variability expressed as WD and DW, especially in monsoon margins (H5, H6), orographic transition zones, and high latitudes (H3).

Large-scale land-surface controls and climate associations with the DD–WW paradigm

The four transition states were unevenly distributed across land cover types (Fig. 3a, c). DD was most common in cropland and urban areas, occupying 35.69% and 35.67% of these regions, respectively, and remained relatively high in forests at 34.80%. Conversely, wetlands had the lowest DD proportion (31.71%) and the highest dry-to-wet transitions (DW) (30.45%). Barren lands showed a share of wet-to-dry transitions (WD) of 30.20%, while shrub/grass/savanna areas were more evenly distributed among the four transition categories. These patterns suggest that land surface properties influence the translation of atmospheric wetting and drying signals into hydrological responses. Wetlands, with their higher storage capacity and buffering, align with the higher DW share, whereas barren areas, with limited infiltration and weak subsurface storage, may reduce the efficiency of converting climatic wetting into hydrological recovery, thus favoring WD. Higher DD fractions in croplands and urban areas are also plausible, as land conversion and impervious surfaces can increase runoff, decrease infiltration and recharge, and sustain hydrological persistence under drying conditions. These findings align with broader evidence that land-cover changes affect runoff, infiltration, and groundwater recharge, with wetlands and urban surfaces representing contrasting extremes in the storage–runoff spectrum (*19*, *20*).

The irrigation analysis provided a more specific anthropogenic perspective. Globally, the proportion of WD increased from 23.66% in areas with very low irrigation to 34.21% in highly irrigated regions, whereas DW decreased from 23.21% to 14.70% (Fig. 3b, d).

https://doi.org/10.5194/egusphere-2026-4696
Preprint. Discussion started: 18 August 2026

DD was most prevalent in low-to-moderate irrigation zones (33.40% and 32.67%, respectively) and was less prevalent in the highest irrigation zone (26.06%). When focusing on croplands, a similar trend was observed: DD decreased from 38.43% in low-irrigation croplands to 32.63% in highly irrigated croplands, WD increased from 18.66% to 27.82%, and DW decreased from 22.56% to 15.72%. This pattern indicates that higher irrigation intensity does not simply lead to increased hydrologic wetting, but rather reflects a redistribution across transition states, with less persistent drying and a stronger inclination toward WD. The explanation for this phenomenon is that irrigation modifies land–atmosphere and surface–water balances to buffer drying signals and increase the decoupling between climate and hydrology. Increased irrigation may weaken DD persistence but does not lead to sustained wetting. Previous studies have shown that irrigation can alter evapotranspiration, energy partitioning, runoff, and land–atmosphere coupling (*21*–*23*).

Climate-related analysis indicated that this interannual variability was linked to large-scale ocean–atmosphere fluctuations, although not in a manner that permits formal attribution. In the annual correlations, WW was negatively associated with PDO, AO, and NOI, whereas WD was positively associated with all three indices (Fig. S2). DD exhibited the strongest negative correlation with AO, and DW showed the strongest positive correlation with AO and a weaker positive correlation with PDO. The phase comparison supports this pattern: positive PDO and AO phases corresponded to larger fractions of WD and DW and smaller fractions of WW and DD, whereas positive NOI aligned with larger DD and WD but smaller WW and DW. Given the modest correlation magnitudes, these relationships should be interpreted as indications of large-scale climatic associations that support a physical interpretation rather than direct causality. SOI composites add context to these transition states. Years with high values across all four classes mostly coincided with negative SOI anomalies, with the most negative global-mean SOI during DW and WW years and the least negative during WD years (Fig. S2d–g). Negative SOI values are indicative of an El Niño–like atmospheric background; therefore, the composites suggest that widespread transitions tend to occur within a broadly negative SOI environment, although the intensity of that background varied among the four classes.

Overall, the results showed that the transition states reflected the long-term hydroclimatic regime, whereas the year-to-year prevalence of WW, DD, WD, and DW was correlated with broader atmospheric and oceanic variability. The clearest signal was from AO, particularly in its negative association with DD and positive association with DW, whereas PDO exhibited a weaker but consistent contrast between the persistent and transition states. NOI displayed a more selective pattern centered on WD and DD. This indicates that both annular-mode variability and Pacific decadal variability are known to reorganize circulation and hydroclimatic anomalies, and that the SOI reflects the large-scale atmospheric component of the El Niño–Southern Oscillation (*24*, *25*).

Future scenarios of the DD–WW paradigm

Under future warming, wet patterns will remain widespread, but the spatial organization of transition states will vary by timescale, period, and emission pathways (Figs. 4 and S3). During SSP585, the mid-century period (2041–2060) exhibited broader large-scale stability, especially across Europe, North America, sub-Saharan Africa, and parts of Asia, while more transitional behaviors (WD and DW) continued in South Asia and the Sahel (Fig. 4a, b, c, d). On the shorter SPEI-3 timescale, the transition structure showed greater spatial variability, whereas the longer SPEI-12 timescale displayed a more unified pattern, with fewer WD and DW transitions and a clearer division between persistent

https://doi.org/10.5194/egusphere-2026-4696
Preprint. Discussion started: 18 August 2026

WW and DD regions (Fig. 4). In northern latitudes, WW trends were predominant, whereas in semiarid regions, DD became more prominent, indicating that the temporal scale strongly affected the detection of transient versus persistent hydroclimatic responses. The SSP585 ensemble further emphasized these differences across timescales and periods (Fig. 4). On the shorter timescale, WW increased from 28.8% in 2041–2060 to 35.2% in 2081–2099, DD increased from 18.6% to 24.4%, WD decreased from 20.8% to 13.7%, and DW decreased from 31.9% to 26.7%. Over the long term, WW increased from 29.1% to 36.2%, DD increased from 17.9% to 22.3%, WD decreased from 20.4% to 12.7%, and DW decreased from 32.6% to 28.7%. Both timescales suggest a trend toward more persistent wetting and drying conditions in the late century, with diminishing transitional states. The regional responses under the moderate emissions scenario (SSP245) showed greater variability across different scales. However, additional analysis indicated a consistent trend of sustained WW and DD states with fewer transitional WD and DW states, particularly at longer timescales (Fig. S3).

Kernel density estimation-based smoothed evaporation (ΔE) and precipitation (ΔP) anomalies across six major river basins (e.g., Amazon, Yangtze, Ganges, Nile, Mississippi, and Murray-Darling) exhibited stronger drying trends throughout under SSP585, with intense WD > DD transitions prevalent within the Amazon, Ganges, and Mississippi Basins (Figs. S4–S5: Supplementary Information: S2.2). In contrast, a more balanced transition, with some wetting patterns retained in the Amazon, Yangtze, and Nile Basins, was used in SSP245. The DW and WD classifications showed greater variability, particularly in the semi-arid regions (such as South Asia and southern Africa) (Fig. 4). These classifications highlight the seasonal variability induced by moderate emissions and their sensitivity to emission pathways in semi-arid and monsoon-dependent areas. However, the larger scale was more compact, with more apparent boundaries between the DD and WW trends (Fig. 4). A dominant WW trend was observed in northern Europe, while DD trends were amplified in arid regions, such as the Sahel (*26*, *27*). The responses of the WD and DW classifications were more variable, especially in dynamic areas (e.g., southern Africa and Central America). The extent of this high variability reflects the near-term uncertainties that are associated with extreme emission scenarios.

Discussion and implications

The DD–WW paradigm describes hydrological changes in historical and future periods. The global application of the DD–WW paradigm does not adequately capture the range and types of land hydrological responses to climate forcing. A regional hotspot breakdown showed that area-specific effects of changing precipitation patterns caused dryness. Southern Europe's transition toward dryness is consistent with the projected increasing aridity of the Mediterranean (*28*) through water availability and agricultural production concerns. The combination of WD and DD in northern Africa reflects increasing aridity and drought vulnerability (*29*, *30*). These trends are particularly concerning, given the region's existing water stress and reliance on scarce water resources. In contrast, sub-Saharan Africa exhibits a mix of DW and WW, suggesting some relief from wet conditions and the potential for improved water availability. However, these trends are insignificant, indicating that hydrological changes in the region are variable and complex. These results suggest that DD–WW changes are occurring, but these variations are not sufficient to confidently be attributed to long-term trends; data uncertainty or internal variability may play a role in these results (*5*). However, the observed wetness may affect agriculture, water resource management, and flood risk. The drying trends are accentuated in the high-emissions SSP scenario (Fig. 4), as observed in the Amazon for the 2081–2099 period, with dominant wet-to-dry

https://doi.org/10.5194/egusphere-2026-4696
Preprint. Discussion started: 18 August 2026

transitions. A decrease in monsoon reliability is associated with water stress, and this "wet-to-dry" trend is more pronounced under the SSP585 scenario than under the SSP245 scenario. The mixed transitions indicate regional variability resulting from local climate patterns and differing water management practices in the agricultural and land-use regions (L2 and L4).

The SSPs showed increased numbers of WD transitions with stronger signals, as reported by (*31*, *32*). These transitions are particularly concerning, as they indicate shifts in water availability that could exacerbate drought risks and reduce the resilience of ecosystems and agricultural systems. These findings are consistent with those of a previous study (*33*), indicating similar dry patterns. The risks associated with climate change are increasing, and scale-dependent variations in risk provide insights into the short- and long-term climatic impacts under both SSPs. This aligns with the results of subsequent studies, that is, (*34*), SSP-based climate response, and (*35*) on controls on global precipitation under global warming. Historical WW patterns account for 47.1% of the global land area, while 22.7% of the global land area is transitioning from wet conditions to drier conditions: the "drier in dry, wetter in wet" paradigm. Under SSP585, the WD transition is less than the historical transition, ranging between 20.8% (2041–2060) and 13.7% (2081–2099). In our study, this value was slightly larger than those in previous studies (*10*, *13*), suggesting that different data and methods affected the coverage of the transitional areas.

The regional response varies significantly under the SSP245 scenario. Large DW and WD transitions occurred at short-term SPEI-SR scales, primarily in regions with monsoon climates (South Asia) (*36*, *37*) and transitional zones (Sahel) (*38*). Divergent responses are distinct in terms of vulnerability across temporal scales in Africa. Localized variability in DW and WD classifications is evident in transitional zones, such as the Sahel, at finer temporal scales (Figures S6–S9). However, a significantly stronger dominance of DD over longer periods indicates long-term drought hazards associated with medium and high emissions. This finding agrees with that of (*39*), who reported increased drought risk in these regions under warming scenarios and suggested that short- and long-term responses must be considered. The differences observed between the two scales suggest that assessing climate at different temporal resolutions can isolate a comprehensive range of climatic responses. Smaller scales offer insight into more localized, short-term variability and provide critical information for understanding immediate climatic impacts and refining adaptation strategies. However, a larger scale provides long-term trends, regional stability, and a broader outlook, given the systemic impact of the emission pathways. Taken together, these analyses reveal how divergence occurs under multiple SSPs, highlighting the urgency for robust mitigation strategies to address both near- and long-term climate risks.

The findings underscore that both statistically significant and nonsignificant trends in hydrological changes should be considered. Significant trends provide robust evidence of the occurrence of changes (Fig. 1). Nevertheless, nonsignificant trends indicate that changes have occurred (in general) without the consistency or strength required to achieve statistical confidence. Although the resulting trends are significant and nonsignificant, these patterns suggest emerging trends and guide adaptive management strategies for river basins, where declines have been reported and may continue under climate change (*40*). Thus, the significance of these observations is considerable, as this study provides a basis for historical and future periods, and could also serve as a constraint for regional and global studies in this domain. However, the direct consequences for water resource management, agriculture, and ecosystems include trends in wetness and dryness, which remain challenging. Increased wetness poses

https://doi.org/10.5194/egusphere-2026-4696
Preprint. Discussion started: 18 August 2026

flooding and waterlogging risks in some regions, while a shift toward dryness increases drought and water scarcity risks globally. These trends highlight that spatial variability necessitates water resource management and climate adaptation at local scales, informed by the specific challenges and opportunities of each region and supported by more robust, consistent data. However, multimodal ensemble simulations can improve estimates of the WW–DD paradigm, thus reducing uncertainty.

Overall, the global patterns of the WW, DD, WD, and DW states can be best understood as the combined result of persistent hydroclimatic background conditions and their modulation by land-surface and large-scale climate variability. Although persistent drying primarily drives the overall global transition structure, reversals between wetting and drying remain common and play a significant dynamic role. Land-surface analysis revealed that factors such as vegetation cover, wetland storage, cropland extent, urban surfaces, and irrigation affect the translation of climatic signals into hydrological responses. Climate diagnostics indicate that the year-to-year variability of these transition states is linked to broad ocean–atmosphere patterns, especially the AO and, to a lesser extent, the PDO, NOI, and SOI. These findings offer a more physically grounded understanding of global hydroclimatic transitions and demonstrate that their spatial and temporal variability is shaped by persistent climatic tendencies and the land-surface and atmospheric conditions under which they occur.

Compliance with Ethics Requirements

This work does not contain any studies with human or animal subjects.

Data and Code Availability Statement

All data are available in the main text or the supplementary materials." No specific code or software was used for data collection; for data analysis and plotting, Python 3.12.3 libraries are used: "netCDF4", "pandas", "numpy", "scipy.interpolate", "matplotlib.pyplot", "xarray", "geopandas", "rioxarray", "cartopy.crs", "cartopy.feature", "sklearn.ensemble", "sklearn.metrics", "sklearn.model_selection", "RandomForestRegressor", "climate-indices". Also, the code used to produce the figures could be obtained from the first author (faiz_ma@neau.edu.cn) upon reasonable request.

Conflict of interest

All authors declare no financial or non-financial competing interests

Declaration of AI used

The authors used Grammarly Pro for language editing.

Author's Contribution:
MAF: Conceived and designed the experiments, analyzed the data, contributed materials/analysis tools, wrote the paper; DL: Analyzed the data, Contributed materials/analysis tools, wrote the paper; LZ, QF, ML, XQ, TL, SC: Contributed materials/analysis tools, wrote the paper.

https://doi.org/10.5194/egusphere-2026-4696
Preprint. Discussion started: 18 August 2026

Acknowledgments:

This study is supported by the Program for Young Talents of Basic Research in Universities of Heilongjiang Province (No. YQJH2025015), National Key R&D Program of China (2023YFD1501004), National Natural Science Foundation of China (52179008, 52309012, 51579044, 41071053), and the Joint Guidance Project of Heilongjiang Natural Science Foundation (LH2023E003). We appreciate the editors and anonymous reviewers for their critical comments, which have improved the quality of the paper.

REFERENCES

1. A. K. Mishra, V. P. Singh, A review of drought concepts. *Journal of hydrology* **391**, 202–216 (2010).
2. T. R. Ault, On the essentials of drought in a changing climate. *Science* **368**, 256–260 (2020).
3. A. B. Smith, J. L. Matthews, Quantifying uncertainty and variable sensitivity within the US billion-dollar weather and climate disaster cost estimates. *Nat Hazards* **77**, 1829–1851 (2015).
4. J. A. Otkin, M. C. Anderson, C. Hain, M. Svoboda, D. Johnson, R. Mueller, T. Tadesse, B. Wardlow, J. Brown, Assessing the evolution of soil moisture and vegetation conditions during the 2012 United States flash drought. *Agricultural and forest meteorology* **218**, 230–242 (2016).
5. M. Hoerling, A. Kumar, The Perfect Ocean for Drought. *Science* **299**, 691–694 (2003).
6. K. E. Trenberth, A. Dai, G. Van Der Schrier, P. D. Jones, J. Barichivich, K. R. Briffa, J. Sheffield, Global warming and changes in drought. *Nature Climate Change* **4**, 17–22 (2014).
7. A. Dai, Increasing drought under global warming in observations and models. *Nature climate change* **3**, 52–58 (2013).
8. C. Chou, J. C. Chiang, C.-W. Lan, C.-H. Chung, Y.-C. Liao, C.-J. Lee, Increase in the range between wet and dry season precipitation. *Nature Geoscience* **6**, 263–267 (2013).
9. H. Feng, M. Zhang, Global land moisture trends: drier in dry and wetter in wet over land. *Scientific reports* **5**, 18018 (2015).
10. P. Greve, B. Orlowsky, B. Mueller, J. Sheffield, M. Reichstein, S. I. Seneviratne, Global assessment of trends in wetting and drying over land. *Nature geoscience* **7**, 716–721 (2014).
11. J. K. Roundy, C. R. Ferguson, E. F. Wood, Temporal variability of land–atmosphere coupling and its implications for drought over the southeast United States. *Journal of Hydrometeorology* **14**, 622–635 (2013).
12. X. Zhang, F. W. Zwiers, G. C. Hegerl, F. H. Lambert, N. P. Gillett, S. Solomon, P. A. Stott, T. Nozawa, Detection of human influence on twentieth-century precipitation trends. *Nature* **448**, 461–465 (2007).
13. H. Feng, M. Zhang, Global land moisture trends: drier in dry and wetter in wet over land. *Scientific reports* **5**, 18018 (2015).

https://doi.org/10.5194/egusphere-2026-4696
Preprint. Discussion started: 18 August 2026

14. B. I. Cook, E. R. Cook, J. E. Smerdon, R. Seager, A. P. Williams, S. Coats, D. W. Stahle, J. V. Díaz, North American megadroughts in the Common Era: reconstructions and simulations. *WIREs Climate Change* **7**, 411–432 (2016).

15. Y. Pokhrel, F. Felfelani, Y. Satoh, J. Boulange, P. Burek, A. Gädeke, D. Gerten, S. N. Gosling, M. Grillakis, L. Gudmundsson, Global terrestrial water storage and drought severity under climate change. *Nature Climate Change* **11**, 226–233 (2021).

16. J. T. Abatzoglou, S. Z. Dobrowski, S. A. Parks, K. C. Hegewisch, TerraClimate, a high-resolution global dataset of monthly climate and climatic water balance from 1958–2015. *Scientific data* **5**, 1–12 (2018).

17. M. C. Anderson, C. A. Zolin, P. C. Sentelhas, C. R. Hain, K. Semmens, M. T. Yılmaz, F. Gao, J. A. Otkin, R. Tetrault, The Evaporative Stress Index as an indicator of agricultural drought in Brazil: An assessment based on crop yield impacts. (2016).

18. M. Zhao, G. A, I. Velicogna, J. S. Kimball, Satellite observations of regional drought severity in the continental United States using GRACE-based terrestrial water storage changes. *Journal of Climate* **30**, 6297–6308 (2017).

19. I. Åhlén, J. Thorslund, P. Hambäck, G. Destouni, J. Jarsjö, Wetland position in the landscape: Impact on water storage and flood buffering. *Ecohydrology* **15**, e2458 (2022).

20. J. Chen, L. Theller, M. W. Gitau, B. A. Engel, J. M. Harbor, Urbanization impacts on surface runoff of the contiguous United States. *Journal of environmental management* **187**, 470–481 (2017).

21. R. Harding, E. Blyth, O. Tuinenburg, A. Wiltshire, Land atmosphere feedbacks and their role in the water resources of the Ganges basin. *Science of the Total Environment* **468**, S85–S92 (2013).

22. Y. Lu, K. Harding, L. Kueppers, Irrigation effects on land–atmosphere coupling strength in the United States. *Journal of Climate* **30**, 3671–3685 (2017).

23. Q. Xia, P. Liu, Y. Fan, L. Cheng, R. An, K. Xie, L. Zhou, Representing irrigation processes in the land surface-hydrological model and a case study in the Yangtze river Basin, China. *Journal of Advances in Modeling Earth Systems* **14**, e2021MS002653 (2022).

24. M. Newman, M. A. Alexander, T. R. Ault, K. M. Cobb, C. Deser, E. Di Lorenzo, N. J. Mantua, A. J. Miller, S. Minobe, H. Nakamura, The Pacific decadal oscillation, revisited. *Journal of Climate* **29**, 4399–4427 (2016).

25. S. Vazifehkhah, E. Kahya, Hydrological drought associations with extreme phases of the North Atlantic and Arctic Oscillations over Turkey and northern Iran. *International journal of Climatology* **38**, 4459–4475 (2018).

26. European Environment Agency, Wet and dry — heavy precipitation and river floods. https://www.eea.europa.eu/publications/europes-changing-climate-hazards-1/wet-and-dry-1/wet-and-dry-heavy.

27. X. Zhang, J. P. Evans, A. L. Burrell, Less than 4% of dryland areas are projected to desertify despite increased aridity under climate change. *Communications Earth & Environment* **5**, 300 (2024).

https://doi.org/10.5194/egusphere-2026-4696
Preprint. Discussion started: 18 August 2026

28. Y. H. Essa, M. Hirschi, W. Thiery, A. M. El-Kenawy, C. Yang, Drought characteristics in Mediterranean under future climate change. *npj Climate and Atmospheric Science* **6**, 133 (2023).

29. N. Brooks, Drought in the African Sahel: long term perspectives and future prospects. *Tyndall Centre for Climate Change Research Working Paper* **61**, 37 (2004).

30. D. Francis, R. Fonseca, Recent and projected changes in climate patterns in the Middle East and North Africa (MENA) region. *Scientific Reports* **14**, 10279 (2024).

31. B. B. Goswami, S.-I. An, An assessment of the ENSO-monsoon teleconnection in a warming climate. *npj Climate and Atmospheric Science* **6**, 82 (2023).

32. S. Woo, G. P. Singh, J.-H. Oh, K.-M. Lee, Possible teleconnections between East and South Asian summer monsoon precipitation in projected future climate change. *Meteorol Atmos Phys* **131**, 375–387 (2019).

33. W. Dorigo, R. De Jeu, D. Chung, R. Parinussa, Y. Liu, W. Wagner, D. Fernández-Prieto, Evaluating global trends (1988–2010) in harmonized multi-satellite surface soil moisture. *Geophysical Research Letters* **39**, 2012GL052988 (2012).

34. B. C. O'Neill, C. Tebaldi, D. P. Van Vuuren, V. Eyring, P. Friedlingstein, G. Hurtt, R. Knutti, E. Kriegler, J.-F. Lamarque, J. Lowe, The scenario model intercomparison project (ScenarioMIP) for CMIP6. *Geoscientific Model Development* **9**, 3461–3482 (2016).

35. G. L. Stephens, T. D. Ellis, Controls of global-mean precipitation increases in global warming GCM experiments. *Journal of Climate* **21**, 6141–6155 (2008).

36. A. Kitoh, The Asian monsoon and its future change in climate models: A review. *Journal of the Meteorological Society of Japan. Ser. II* **95**, 7–33 (2017).

37. A. G. Turner, H. Annamalai, Climate change and the South Asian summer monsoon. *Nature Climate Change* **2**, 587–595 (2012).

38. S. Salack, C. Klein, A. Giannini, B. Sarr, O. N. Worou, N. Belko, J. Bliefernicht, H. Kunstman, Global warming induced hybrid rainy seasons in the Sahel. *Environmental Research Letters* **11**, 104008 (2016).

39. N. S. Diffenbaugh, D. L. Swain, D. Touma, Anthropogenic warming has increased drought risk in California. *Proc. Natl. Acad. Sci. U.S.A.* **112**, 3931–3936 (2015).

40. Y. Zhang, H. Zheng, X. Zhang, L. R. Leung, C. Liu, C. Zheng, Y. Guo, F. H. Chiew, D. Post, D. Kong, Future global streamflow declines are probably more severe than previously estimated. *Nature Water* **1**, 261–271 (2023).

https://doi.org/10.5194/egusphere-2026-4696
Preprint. Discussion started: 18 August 2026

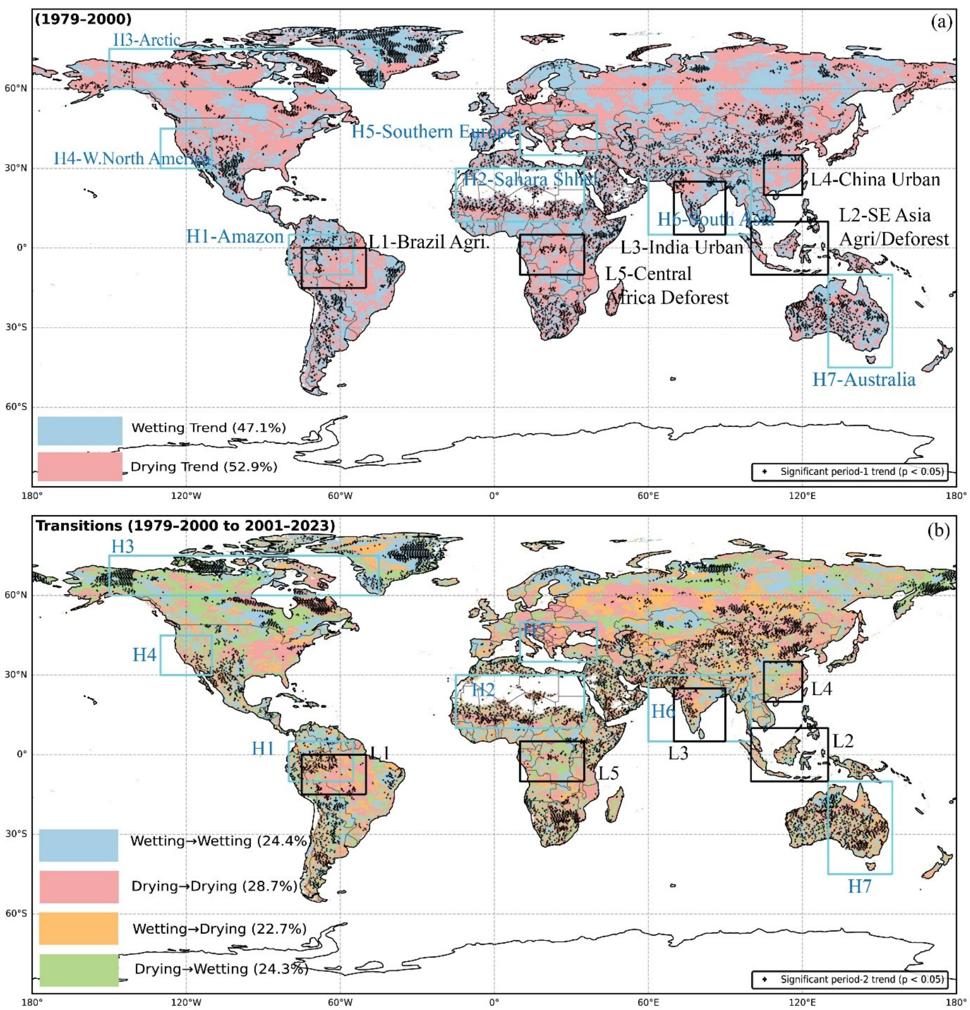

Fig. 1: Dry–dry (DD), wet–wet (WW), and DD–WW paradigm classification, with transitions from wet to dry (WD) and dry to wet (DW). a) SPEI-SR 3-month scale linear trend for the period 1979–2000, based on values greater than or less than 0 (>0 = wet, <0 = dry); b) SPEI-SR 3-month scale linear trend based for the baseline period 1979–2000 extended to 2001–2023, indicating whether the areas are transitioning from wet to dry or dry to wet relative to the baseline period. Percentages represent the proportion of grid points in each category. Solid boxes indicate synthetic hotspots H1–H7: H1 Amazon; H2 Sahara–Sahel; H3 Arctic; H4 Western North America; H5 Southern Europe; H6 South Asia; and H7 Australia. Black boxes indicate land-use domains L1–L5: L1 Brazil Agriculture; L2 SE Asia Agriculture/Deforestation; L3 India Urban; L4 China Urban; and L5 Central Africa Deforestation.

https://doi.org/10.5194/egusphere-2026-4696
Preprint. Discussion started: 18 August 2026

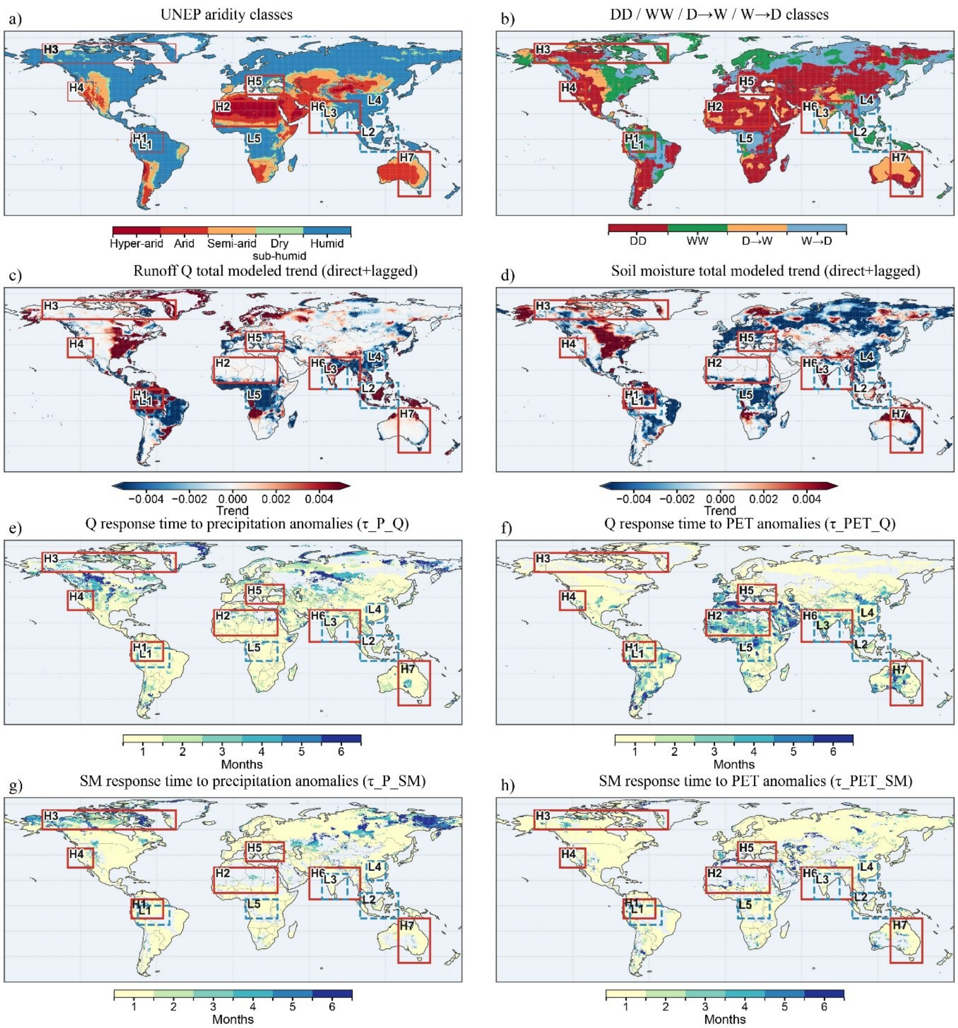

Fig. 2: (a) UNEP aridity classes (hyper-arid to humid). (b) DD/WW taxonomy based on the UNEP dryness split (AI_UNEP < 0.65). (c–d) Total modeled trends in Q and SM (direct and lagged components). (e–h) Response times (τ, months) of Q and SM to P′ and PET′, respectively. Red solid boxes indicate synthetic hotspots H1–H7: H1 Amazon; H2 Sahara–Sahel; H3 Arctic; H4 Western North America; H5 Southern Europe; H6 South Asia; H7 Australia. Blue dashed boxes indicate land-use domains L1–L5: L1 Brazil Agriculture; L2 SE Asia Agriculture/Deforestation; L3 India Urban; L4 China Urban; L5 Central Africa Deforestation.

https://doi.org/10.5194/egusphere-2026-4696
Preprint. Discussion started: 18 August 2026

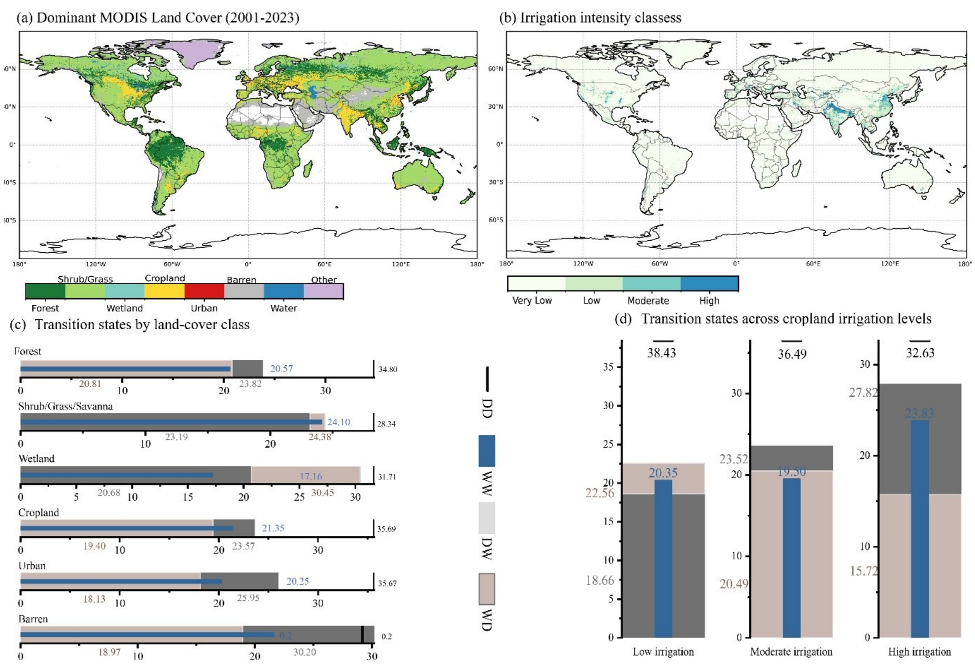

Fig. 3: Land-surface controls on the DD–WW paradigm. (a) Dominant MODIS land-cover class during 2001–2023. (b) Irrigation-intensity classes derived from FAO GMIA v5. (c) Area-weighted distribution of transition states across major land-cover classes. (d) Area-weighted distribution of transition states across cropland irrigation levels.

https://doi.org/10.5194/egusphere-2026-4696
Preprint. Discussion started: 18 August 2026

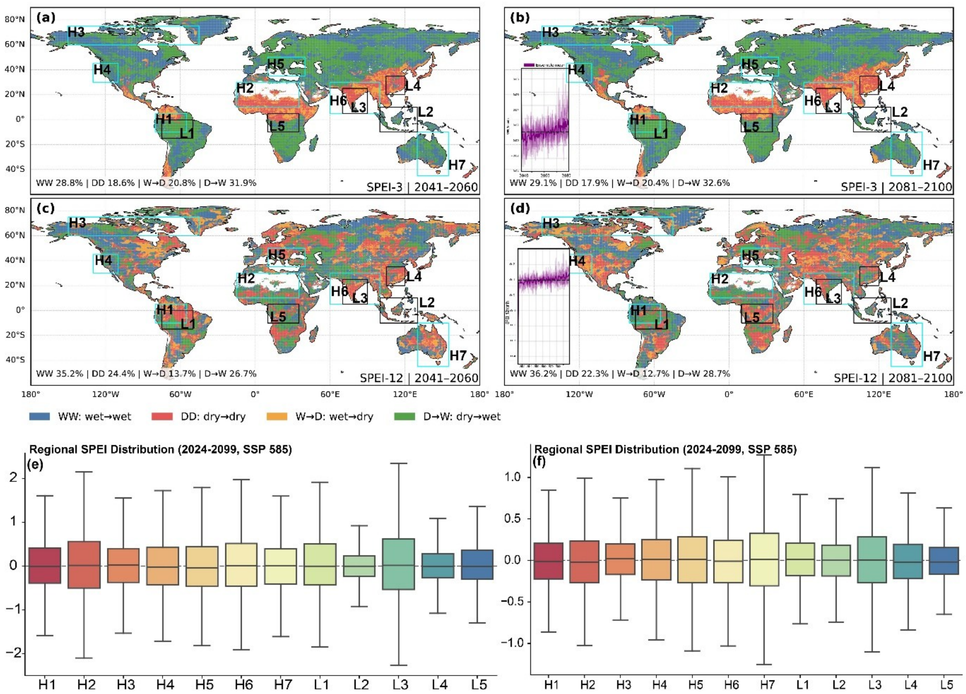

Fig. 4: Future hydroclimatic transition states under SSP585 across short (3-month) and long (12-month) SPEI timescales. The figure shows ensemble transition states for SPEI-3 and SPEI-12 during 2041–2060 and 2081–2100, compared to the 1979–2023 baseline. WW indicates wet-to-wet persistence, DD dry-to-dry persistence, WD wet-to-dry transitions, and DW dry-to-wet transitions. Insets show the ensemble mean SPEI time series, while box plots depict regional SPEI distributions in selected hotspot and lower-signal regions.